

# Half-Space Power Diagrams and Discrete Surface Offsets\*

Zhen Chen, Daniele Panozzo, Jérémie Dumas

**Abstract**—We present a novel algorithm to compute offset surfaces of shapes discretized using a *dexel* data structure that is both fast and trivially parallel. We achieve this by exploiting properties of *half-space* power diagrams, where each seed is only visible by a half space. This allows us to develop a two-stage sweeping algorithm that is both simple to implement and efficient, and avoids computing a 3D volumetric distance field. The primary application of our method is interactive modeling for digital fabrication, where printed objects have a finite resolution. However, our method can also be used for other purposes where a fast but approximate offset solution is desirable. We present experimental timings, how they compare with previous approaches, and provide a reference implementation in the supplemental material.

**Index Terms**—Geometry Processing, Offset, Voronoi Diagram, Power Diagram, Dexels, Layered Depth Images.

## 1 INTRODUCTION

Morphological operations such as dilation and erosion have numerous applications in various areas of computer science. They can be used to regularize shapes [1], ensure robust designs in topology optimization [2], perform collision detection [3], or compute image skeletons [4]. Surface offsetting operations are also extremely useful in the context of digital fabrication [5]: erosion can be used to generate support structures [6], to hollow an object or create a mold, closing operations can remove small holes in a model, etc.

While offset surfaces can be computed exactly by way of Minkowski sums [7], these operations can be fairly slow, especially on large models. Recent approaches [8] can provide better results, but performances are still a concern, limiting their use in interactive applications. Conversely, approximate algorithms that rely on a discrete re-sampling of the input volume can lead to more efficient solutions, while sacrificing accuracy [9], [10] in a controlled way. This is especially interesting for applications in digital fabrication, where the resolution is anyhow limited by the machines and it is thus unnecessary to achieve infinite accuracy.

We present a novel algorithm to compute offset surfaces on a ray-based representation (ray-rep) of a solid. A ray-rep, such as the *dexel buffer*, stores the intersection results of a solid object with a set of parallel rays in a uniform 2D grid – each cell of the grid holds a list of *intervals* bounding the solid, as illustrated Figure 2. Ray-reps are extremely appealing in the context of digital fabrication, as they allow us to perform a number of operations directly in image-space, at the resolution of the machine. The computed result is thus identical to what is obtained by solving the problem exactly and then rounding it to machine resolution, but at a fraction of the cost. This includes CSG operations, but also support other common tasks such as support detection,

toolpath palling, and infill calculations. Implicit surfaces can also be discretized directly without prior explicit meshing. Examples in the literature can be found for Computer Numerical Control (CNC) milling applications [11], modeling for additive manufacturing [12], hollowing, or contouring [5]. The offset algorithm we present in this article is both fast and *accurate*, in that it computes the *exact* offset of its input discrete dexel structure, in contrast to existing methods such as [10]. Our algorithm is also embarrassingly parallel, and its complexity scales well with the offset radius.

Our algorithm relies on a novel way to compute half-plane Voronoi diagrams [13]. We first discuss the 2D case and present a simple and efficient sweeping algorithm to compute offsets in a 2D dexel structure. We then extend our sweeping procedure from 2D to 3D by leveraging the separability of the Euclidean distance, similarly to existing signed-distance function algorithms [14].

In Section 4, we compare running times of our algorithm

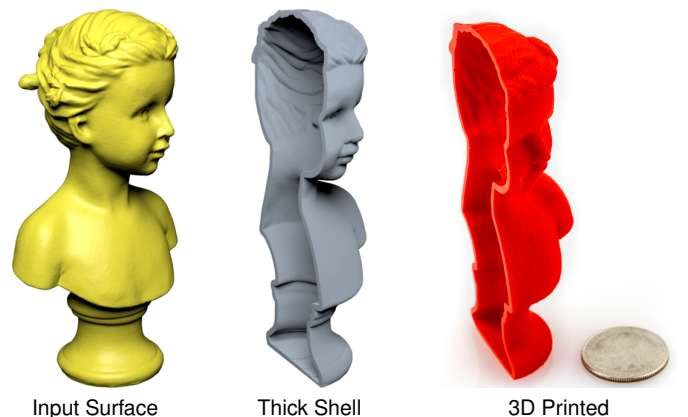


Fig. 1. 3D printed surface shell, computed with our approach. The shell is the Boolean difference of a dilation and an erosion of the input volume. The model uses a grid of  $512^2$  dexels, and a dilation radius of 4 dexels.

\*. This work has been submitted to the IEEE for possible publication. Copyright may be transferred without notice, after which this version may no longer be accessible.

with existing approaches, and discuss existing methods. Finally, we show different applications of our approach, including topological simplification and modeling for additive manufacturing.

## 2 RELATED WORK

**Exact Mesh Offsets.** If the input shape is represented as a triangle mesh, a way to compute a dilated surface is to resolve the self-intersection in the raw offset surface [15]. In general, a dilated mesh can also be obtained by computing the Minkowski sum of the input triangle mesh and a sphere of the desired radius [7]. This approach, which is implemented robustly in CGAL, can become slow for large models with complex geometry. Other algorithms avoiding the use of arbitrary precision arithmetic have been proposed to extract the boundary polygons of a Minkowski sum [16]. Still, those methods are sensitive to the quality and complexity of the input mesh, and do not provide interactive runtimes.

**Resampled Offsets.** Rather than extracting the boundary of the Minkowski sum directly, which is a challenging and time-consuming operation, other methods chose to resample the offset surface, by computing the isosurface of the signed-distance function to the original surface [17], [18]. A more recent approach by Meng *et al.* [8] distribute and optimize the position of sites at a specified distance from the original surface, and produces a triangle from a restricted Delaunay triangulation of the sites. Calderon *et al.* [19] introduced a framework for performing morphology operations directly on point sets.

**Voronoi Diagrams and Signed-Distance Transforms.** Our algorithm rely on the implicit computation of Voronoi and power diagrams of points and segments. Centroidal tessellations of Voronoi and power diagrams have important application in geometry processing and remeshing [20], [21].

In a method proposed by [22] to a 2D Voronoi diagram of a point set, a sweep line algorithm is employed to position of the Voronoi vertices (intersection of 3 bisectors) that form the Voronoi diagram. By relying on a slight modification of the Voronoi diagram definition, called half-space Voronoi diagrams [13], we will see in Section 3 how to compute the Voronoi diagram of a set of parallel segments directly, using two sweeps instead of one, and how it lead to the efficient computation of a discrete offset surface. The extension of our method to 3D will require the computation of power diagrams [23], where each seed is associated a different weight. Note that our algorithm implicitly relies on the Voronoi and power diagrams of line segments. And while those can be efficiently approximated by sampling each segments with multiple points [24], we will see how to circumvent the approximation entirely and keep the implementation simple.

Finally, our 3D twos-stage sweeping algorithm bears some similarity to existing signed-distance transform approaches such as [14], [25], as it leverages the separability of the Euclidean distance to compute the resulting offset by sweeping in two orthogonal directions. However, as we operate on a

dexel structure, we never need to store a full 3D distance field in memory. For a more complete review of distance transform algorithms, the reader is referred to the survey [26].

**Ray-Based Representations and Offsets.** A ray-based representation of a shape is obtained by computing the intersection of a set of rays with the given shape. In most applications, the cast rays are parallel and sampled on a uniform 2D grid, then stored in a structured called a *dexel buffer*. A dexel buffer is simply a 2D array, where each cell contains a list of *intersection* events ( $z^+$ ,  $z^-$ ) containing the segments intersecting with the solid. See Figure 2 for an illustration. To the best of our knowledge, the term dexel (for *depth pixel*) can be traced back to [11], which introduced the dexel buffer to compute the results of CSG operations to facilitate NC milling path-planning. Similar data structures have been described in different context over the year. *Layered Depth Images* (LDI) [27] are used to achieve efficient image-based rendering. The A-buffer [28], [29] was used to achieve order-independent transparency. While they may differ in the way they are built, the underlying data structure remains similar. Augmenting ray-reps with normal information, the G-buffer [30] stores a normal in every pixel for further image-processing and NC milling applications. In the context of additive manufacturing, *Layered Depth Normal Images* – LDI with normal information – have been proposed as an alternative way to discretize 3D models [31], [32].

Ray-based data structures offer an intermediate representation between usual boundary representations (such as triangle meshes), and volumetric representations (such as a full or sparse 3D voxel grids). While both 3D images and dexel buffers suffer from uniform discretization errors across the volume, a dexel buffer is cheap to store compared to a full volumetric representation. This allows to discretize with very large dexel-buffer resolutions (1024 to 2048 and more) at a very low cost. Additionally, in the context of digital fabrication, 3D printers and CNC milling have limited precision. Consequently, using a dexel buffer at the resolution of the printer is enough to cover the space of shapes that can be fabricated.

Ray-reps have been used to compute and store the results of Minkowski sums, offsets and CSG operations [33]. Hui [34] use ray-reps to compute the result of a solid sweeping in image-space. In [35], Chen *et al.* use LDNI to offset polygonal meshes, by filtering the result of an initial overestimate of the true dilated shape. Wang *et al.* [9] compute the offset mesh as the union of spheres placed on the points sampled by the LDI. As the dilation radius increases, the number of overlapping spheres quickly increases, and they propose to decompose the dilation in a sequence of dilation with smaller radii. Finally, [10] approximate the dilation by a spherical kernel with the dilation by a zonotope, effectively computing the Minkowski sum of the original shape with a sequence of segments in different directions. The method presented in this paper computes the exact offset of the input ray-rep, as opposed to [10]. It also differs from Wang *et al.* [9] in several aspects. The latter requires a LDI sampled from 3 orthogonal directions, while our method accelerates the offset operation even when a ray-rep from a single direction is available. We

describe other key differences in more details in Section 4.

### 3 METHOD

We first introduce the different concepts and notations in Section 3.1, where we present a general overview of our algorithm for offset computation of ray-reps. In Section 3.2, we describe a 2D version of our method, based on efficiently computing the Voronoi diagram of a set of parallel segments. Then, in Section 3.3, we extend the algorithm to compute the power diagram of a set of parallel segments in 2D, and observe that it is the key to extend our 2D offset algorithm to 3D.

#### 3.1 Definitions and Overview

**Dexel Representation.** A dexel buffer of a shape  $S \subset \Omega$  is a set of parallel segments arranged in a 2D grid, where each cell  $S_{ij}$  of the grid contains a list of segments sharing the same  $xy$  coordinate. More specifically, we discretize  $S$  as  $S \approx \cup_{ij} S_{ij}$  where  $S_{ij} = \{(z_k^-, z_k^+)\}_{k=1}^{n_{ij}}$ . Each segment  $(z_k^-, z_k^+)$  in the same cell  $S_{ij}$  have the same  $xy$  coordinate, and represent the intersections of the input shape  $S$  with a vertical ray at the same  $xy$  coordinate (see Figure 2).

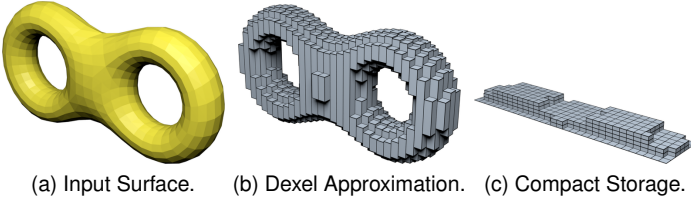


Fig. 2. A dexel data structure constructed from a triangle mesh. The input surface (a) is intersection with evenly spaced parallel rays (b), and stored compactly as a 2D grid of events in the dexel buffer (c). This can be used to perform efficient CSG operations in modeling software [12].

**Dilation.** Given an input shape  $S$  and a radius  $r \geq 0$  we define the *dilated shape*  $\mathcal{D}_r(S)$  as the set of points at distance less than  $r$  from  $S$ :

$$\mathcal{D}_r(S) = \{p \in \Omega, \|p - x\| \leq r, x \in S\} \quad (1)$$

**Erosion.** The erosion of a shape  $S$  is equivalent to computing the dilation on the complemented shape  $\bar{S}$ , and taking the complement of the result. Since the complement operation is trivial under a ray-rep representation, we will focus on describing our algorithm applied to the dilation operation, from which all other morphological operators (erosion, closing, and opening) will follow.

**Voronoi Diagram.** The *Voronoi diagram* of a set of seeds  $\mathfrak{S} = \{s_i\}_{i=1}^n$  is a partition of the space  $\Omega$  into different *Voronoi cells*  $\Omega_i$ :

$$\Omega_i = \{p \in \Omega, \|p - s_i\| \leq \|p - s_j\|, i \neq j\} \quad (2)$$

We also define  $\text{Vor}(\mathfrak{S})$  to be the interface between each overlapping Voronoi cell:

$$\text{Vor}(\mathfrak{S}) = \cup_{i \neq j} \Omega_i \cap \Omega_j \quad (3)$$

When the seeds  $s_i$  are points,  $\text{Vor}(\mathfrak{S})$  is a set of straight line in 2D (planes in 3D), which are equidistant to their closest seeds. When the seeds are segments,  $\text{Vor}(\mathfrak{S})$  is comprised of parabolic arcs in 2D [24], and parabolic surfaces in 3D.

In a half-space Voronoi diagram [13], each seed point  $s_i$  is associated with a *visibility direction*  $v_i$ , and a point  $p$  is considered in Equation (2) if and only if  $(p - s_i) \cdot v_i \geq 0$ . In this work, we are interested in half-space Voronoi diagrams of seed segments, where each seed is associated to the same visibility direction  $v$ . Figure 3 shows the difference between a Voronoi diagram and half-space Voronoi diagrams for point seeds. More precisely, given set of parallel seed segments  $(s_i^-, s_i^+)_{i=1}^n$ , and a direction  $v$  orthogonal to each segment  $v \perp (s_i^+ - s_i^-)$ , we define the half-space Voronoi cells  $\vec{\Omega}_i$  and  $\overleftarrow{\Omega}_i$  as

$$\begin{aligned} \vec{\Omega}_i &= \{p \in \Omega, \|p - \tilde{p}_i\| \leq \|p - \tilde{p}_j\|, i \neq j, \\ &\quad (p - \tilde{p}_i) \cdot v \geq 0, (p - \tilde{p}_j) \cdot v \geq 0\} \\ \overleftarrow{\Omega}_i &= \{p \in \Omega, \|p - \tilde{p}_i\| \leq \|p - \tilde{p}_j\|, i \neq j, \\ &\quad (p - \tilde{p}_i) \cdot v \leq 0, (p - \tilde{p}_j) \cdot v \leq 0\} \end{aligned} \quad (4)$$

where  $\tilde{p}_i$  is the point  $p$  projected on the line  $(s_i^-, s_i^+)$ . Note that the segments  $(s_i^-, s_i^+)$  are parallel and orthogonal to the chosen direction  $v$ , so the dot product  $(p - q) \cdot v$  in Equation (4) has the same sign for all the points  $q$  in the line  $(s_i^-, s_i^+)$ . Note that we have  $\Omega_i \subseteq \vec{\Omega}_i \cup \overleftarrow{\Omega}_i$  (see Figure 3).

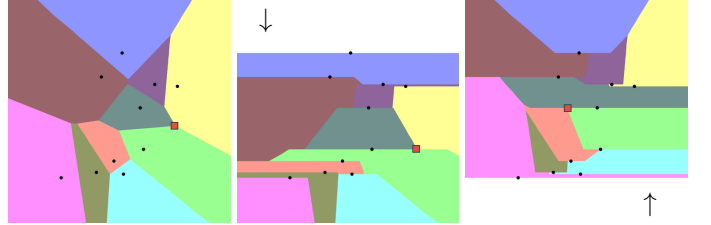


Fig. 3. Voronoi diagram of seed points  $\{s_i\}_{i=1}^n$ . From left to right: Voronoi diagram formed by the full Voronoi cells  $\Omega_i$ ; half-space Voronoi diagram formed by the half-space Voronoi cells  $\vec{\Omega}_i$  and  $\overleftarrow{\Omega}_i$  respectively. Note that  $\Omega_i \subseteq \vec{\Omega}_i \cup \overleftarrow{\Omega}_i$ . In each diagram, one Voronoi vertex (intersection between 3+ Voronoi cells) is shown with a red square.

**Half-Dilated Shape.** We define the *half-dilated shape*  $\vec{\mathcal{D}}(S)$ , as the dilation restricted to the half-space Voronoi cells of segments in  $S$ :

$$\vec{\mathcal{D}}_r(S) = \{p \in \vec{\Omega}_i, \|p - x\| \leq r, x \in s_i, i \in [1, n]\} \quad (5)$$

Remember that  $s_i$  is the  $i$ -th segment  $(z_i^-, z_i^+)$  in the dexel buffer approximating the shape  $S$ . The half-space dilated shape  $\vec{\mathcal{D}}_r(S)$  is defined in a similar manner using  $\vec{\Omega}_i$ . For simplicity, we will omit the dilation radius and simply write  $\mathcal{D}(S)$ , unless there is an ambiguity.

**Power Diagram.** Finally, the *power diagram* of a set of seeds  $\{s_i\}_{i=1}^n$  is a weighted variant of the Voronoi diagram. Each seed is given a weight  $w_i$  that determines the size of the *power cell*  $\Omega_i^p$  associated to it:

$$\Omega_i^p = \left\{p \in \Omega, \|p - s_i\|^2 - w_i \leq \|p - s_j\|^2 - w_j, i \neq j\right\} \quad (6)$$

Intuitively, one could interpret a 2D power diagram as the orthographic projection of the intersection of a set of parabola centered on each seed, where the weights determine the height of each seed embedded in  $\mathbb{R}^3$ . This definition extends naturally to *half-space power diagrams*.

**Overview.** The input of our algorithm is a dixel buffer  $S_{\text{In}}$  and a dilation radius  $r$ . The output is a new dixel buffer  $S_{\text{Out}}$ . A key observation in our approach is that the dilation operation can be separated into two stages. The first stage computes the dilation of the shape  $S_{\text{In}}$  along the Y axis, producing an intermediate shape  $S_{\text{Mid}}$ . Then, the second stage will compute the dilation of  $S_{\text{Mid}}$  along the X axis by a radius  $r$ , producing the final shape  $S_{\text{Out}}$ . This separation  $S_{\text{In}} \rightarrow S_{\text{Mid}} \rightarrow S_{\text{Out}}$  allows us to decompose the two dilation operations into a set of separate 2D dilations along each axis. The first stage, explained in Section 3.2, covers the basic 2D dilation. The second stage (Section 3.3) involves augmenting each ray segment  $(z_i^-, z_i^+, r_i)$  with a weight  $r_i$  that determines the radius of the dilation that should be performed along the second axis in the second stage. This decomposition is illustrated in Figure 4.

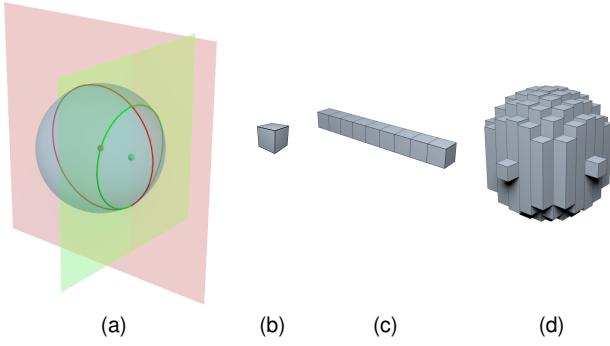


Fig. 4. Dilation operation performed in two stages (a). A seed is dilated by a radius  $r$  along a first axis (in red). The resulting seed (in green) is then dilated along a second axis by a different radius  $\sqrt{d^2 - r^2}$ , where  $d$  is the distance between the two seeds (red point and green point). The equivalent dixel data structure for each pass is shown on right: (b) input dixel, (c) result of the first pass, (d) result of the second pass.

### 3.2 Half-Space Voronoi Diagram of Segments and 2D Offsets

Given a 2D input shape  $S$ , and dilation radius  $r$ , we seek to compute the dilated shape  $\mathcal{D}(S)$ , comprised of the set of points at distance  $\leq r$  from  $S$ . The input shape is given as a union of disjoint parallel segments evenly spaced on a regular grid (the dixel data structure), and we seek to compute the output shape as another dixel structure (the discretized version of the continuous dilated shape).

The dilated shape  $\mathcal{D}(S)$  can be expressed as the union of the dilation of each individual segment of  $S$ . To compute this union efficiently, our key insight is to partition the dilated shape based on the Voronoi diagram of the input segments. Within each Voronoi cell  $\Omega_i$ , if a point  $p$  is at a distance  $\leq r$  from the seed segment  $(s_i^-, s_i^+) \in S$ , then  $p \in \mathcal{D}(S)$ .

The Voronoi diagram of point seeds can be computed in single pass with a sweepline algorithm [22], the construction

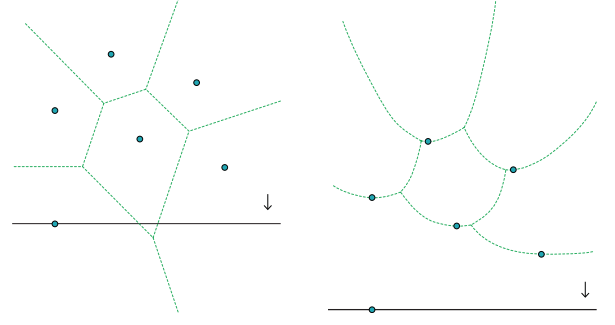


Fig. 5. Fortune's sweepline algorithm [22] requires transforming the point coordinates to compute the correct Voronoi diagram of points in a single sweeping pass, which makes it impossible to compute the result of the dilation in the same sweeping pass.

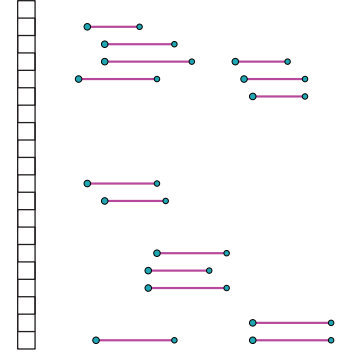


Fig. 6. A single sweep in one direction allows us to compute the half-space Voronoi diagram of parallel line segments (the dixel data structure).

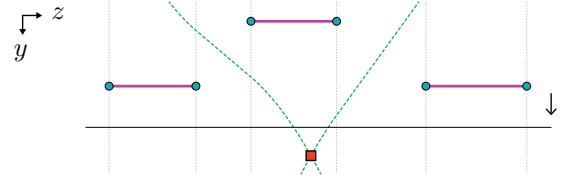


Fig. 7. The bisector of two line segments can be described by a piecewise second-order polynomial curve. Voronoi vertices are located at the intersection between two such bisectors. After this point, the middle segment will always be *further* away from the sweepline than its two neighbors. It will be marked as *inactive* and be removed from  $\mathcal{L}$ .

requires lifting coordinates in the plane according to the coordinate along the sweep direction, as illustrated in Figure 5. Unfortunately, this approach cannot be used to compute the result of a dilation operation in a single pass. Indeed, seeds need to influence the rows *before* and *after* their current position along the sweep direction. Instead, we propose a simple construction for seed points and segments, based on half-space Voronoi diagrams – which we extend to power diagrams in Section 3.3. Our key idea is to compute the dilation of a segment  $(s_i^-, s_i^+)$  in its Voronoi cell  $\Omega_i$  as the union of the two half-dilated segments, in  $\vec{\Omega}_i$  and  $\overleftarrow{\Omega}_i$ . Both  $\vec{\Omega}_i$  and  $\overleftarrow{\Omega}_i$  can be computed efficiently in two separate sweeps of opposite direction, without requiring any transformation to the coordinate system as in [22].

The idea behind our sweeping algorithm is as follows. We advance a sweepline  $L$  parallel to the segments in the input



dexel  $S$  (Figures 6 and 7). At each step, for each seed  $i \in S$ , we compute the intersection of the current line  $L$  with the points in  $p \in \bar{\Omega}_i$  that are at a distance  $\leq r$ . By choosing the visibility direction  $v$  to be the same as the sweeping direction, then only the seeds  $i$  previously encountered in the sweep will contribute to this intersection (upcoming seeds will have an empty Voronoi cell  $\bar{\Omega}_i$ ). Figure 3 shows a Voronoi diagram of points, with two half-space Voronoi diagrams of opposite directions. To make the computation efficient, we do not want to iterate through all the seeds to compute the intersection each time we advance the sweep line (which would make the algorithm  $\mathcal{O}(n^2)$  in the number of seeds). Instead, we want to keep only a small list of *active seeds*, that will contribute to the dilated shape  $\mathcal{D}(S)$  and intersect the current sweepline  $L$ : this will decrease the complexity to  $\mathcal{O}(n \log(n) + m)$ , where  $m$  is the number of segments generated by the dilation process.

**Pseudo-Code.** From an algorithmic point of view, we maintain, during the sweeping algorithm, two data structures:  $\mathcal{L}$ , the list of *active* seed segments  $(s_i^+, s_i^-)$ , whose Voronoi cell  $\bar{\Omega}_i$  intersects the current sweepline (and are at distance  $\leq r$  from the current sweepline), and  $\mathcal{Q}$ , a priority queue of upcoming *events*, that indicates when an active seed can safely be removed from the  $\mathcal{L}$  as we advance the sweepline, i.e. when it no longer affect the result of the dilation. The events in  $\mathcal{Q}$  can be of two types: (1) a Voronoi vertex (the intersection between 3+ Voronoi cells); and (2) a seed becoming inactive due to a distance  $> r$  from the sweepline. Voronoi vertices can be located at the intersection of the bisector curves between 3 consecutive seed segments  $a, b, c \in \mathcal{L}$ , as illustrated in Figure 7. Beyond this intersection, we know that either  $a$  or  $c$  will be closer to the sweepline, so we can remove  $b$  from  $\mathcal{L}$  (its Voronoi cell  $\bar{\Omega}_b$  will no longer intersect the sweepline).

Both  $\mathcal{Q}$  and  $\mathcal{L}$  can be represented by standard STL data structures. Note that since the segments stored in  $\mathcal{L}$  are *disjoint*, they can be stored efficiently in a `std::set<>` (sorted by the coordinate of their midpoint). A detailed description of our sweep-line algorithm is given in pseudo-code in Figures 8 and 9. We also provide a full C++ implementation of our method in supplemental. In line 13, the function `DILATELINE` computed the result of the dilation on the current sweep line, by going through the list of active seeds, and merging the resulting dilated segments. Insertion and removal of seed segments in  $\mathcal{L}$  is handled by the functions `INSERTSEEDSEGMENT` and `REMOVESEEDSEGMENT` respectively. When inserting a new active segment in  $\mathcal{L}$ , to maintain the efficient storage with the `std::set<>`, we need to remove subsegments which are occluded by the newly inserted seed segment (and split partially occluded segments). Indeed, the contribution of such segments is superseded by the new seed segment that is inserted. Then, we need to compute the possible Voronoi vertices formed by the newly inserted seed and its neighboring segments in  $\mathcal{L}$ . The derivation for the coordinates of the Voronoi vertex of 3 parallel seed segments is given in Appendix A.

**Input:** 2D dexel structure  $S$  + dilation radius  $r$ .

**Output:** Half-dilated dexel shape  $S' = \vec{\mathcal{D}}_r(S)$ .

```

1: function VORONOI SWEEP LINE( $S, r$ )
2:    $\mathcal{L} \leftarrow \emptyset$   $\triangleright$  Set of active segments on the sweep line
3:    $\mathcal{Q} \leftarrow \{\}$   $\triangleright$  List of removal events marking a seed as inactive
4:    $S' \leftarrow \emptyset$   $\triangleright$  Dilated result
5:   for  $i \leftarrow 0, N - 1$  do
6:     for all  $s_j \in \mathcal{Q}$  do
7:       REMOVESEEDSEGMENT( $\mathcal{L}, r, s_j$ );
8:     end for
9:     for all  $s_j^i = (z^+, z^-) \in S_i$  do
10:      INSERTSEEDSEGMENT( $\mathcal{L}, \mathcal{Q}, r, s_j$ );
11:    end for
12:     $\triangleright$  Dilate and merge active seeds on the current sweepline
13:     $S' \leftarrow S' \cup \text{DILATELINE}(\mathcal{L}, i, r)$ 
14:  end for
15:  return  $S'$ 
16: end function

```

Fig. 8. Sweepline algorithm for computing the half-dilated shape  $\vec{\mathcal{D}}_r(S)$ .

```

 $\mathcal{L}$    Set of active seeds on the sweep line
 $\mathcal{Q}$    List of removal events
Input:
 $r$     Dilation radius
 $s$     Seed segment to insert,  $s = [(y, z^+), (y, z^-)]$ .
Output: Updated list of active seeds  $\mathcal{L}$  and events  $\mathcal{Q}$ .
1: function INSERTSEEDSEGMENT( $\mathcal{L}, \mathcal{Q}, r, s$ )
2:   REMOVEOCCLUDEDSEGMENTS( $\mathcal{L}, s$ )
3:   SPLITPARTIALLYOCCLUDED( $\mathcal{L}, s$ )
4:    $\mathcal{L} \leftarrow \mathcal{L} \cup s$   $\triangleright$  Overlaps are resolved, insert  $s$  into  $\mathcal{L}$ 
5:    $\mathcal{Q} \leftarrow \mathcal{Q} \cup (y + r, s)$   $\triangleright$  After this point,  $\mathcal{D}_r(s)$  will be empty
6:   while  $\exists$  sequence  $(s_a, s_b, s) \in \mathcal{L}$  do
7:      $(y_v, z_v) \leftarrow \text{VORONOI VERTEX}(s_a, s_b, s)$   $\triangleright$  See fig. 7
8:     if  $y_v < y$  then
9:        $\mathcal{L} \leftarrow \mathcal{L} \setminus s_b$   $\triangleright$  Seed  $s_b$  becomes inactive
10:    else
11:       $\mathcal{Q} \leftarrow \mathcal{Q} \cup (y_v, s_b)$   $\triangleright$  Remove  $s_b$  later on
12:    end if
13:  end while
14:  while  $\exists$  sequence  $(s, s_a, s_b) \in \mathcal{L}$  do
15:     $\triangleright$  Repeat operation on the right side of  $s$ 
16:  end while
17: end function

```

Fig. 9. Insertion of a new seed segment  $s$  into  $\mathcal{L}$ .

### 3.3 Half-Space Power Diagram of Points and 3D Offsets

**3D Dilation.** As illustrated in Figure 4, the 3D dilation process is decomposed in two stages  $S_{\text{In}} \mapsto S_{\text{Mid}} \mapsto S_{\text{Out}}$ . We first perform an extrusion along the first axis (in red), followed by a dilation along the second axis (in green). Note that the first operation  $S_{\text{In}} \mapsto S_{\text{Mid}}$  is not exactly the same as a dilation along the first axis (red plane): the segments  $(s_i^+, s_i^-) \in S_{\text{In}}$  are *extruded*, not dilated (they map to a rectangle, not a disk).

To obtain the final dilated shape in 3D, we need to perform a dilation of the intermediate shape  $S_{\text{Mid}}$ , where each segment  $(s_j^+, s_j^-) \in S_{\text{Mid}}$  is dilated by a different radius  $r_j$  along the second axis (green plane in Figure 4), depending on

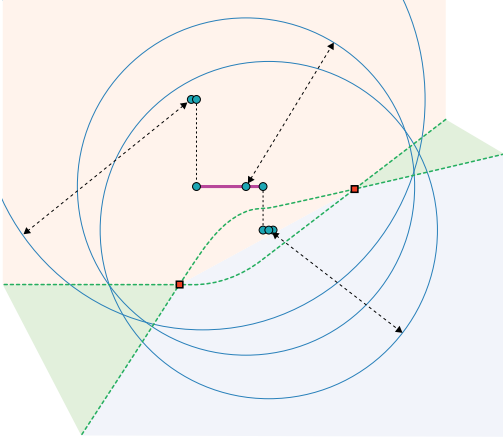


Fig. 10. Special case: the power cell of a seed segment (in green) can be a disconnected region of the plane.

its distance from parent seed (red dot in Figure 4). In the case where the first extrusion of  $S_{\text{In}}$  produces overlapping segments in  $S_{\text{Mid}}$ , the overlapping subsegments would need to be dilated by different radii, depending on which segment in  $S_{\text{In}}$  it originated from. In such a case, where a subsegment  $\tilde{s} \in S_{\text{Mid}}$  has multiple parents  $\tilde{s}_i \in S_{\text{In}}$ , it is enough to dilate  $\tilde{s}_j$  by the radius of its closest parent in  $S_{\text{In}}$  (the one for which  $r_j^i = \sqrt{d_{ij}^2 - r^2}$  will be the largest). In practice, we store  $S_{\text{Mid}}$  as a set of non-overlapping segments, as computed by our algorithm Figure 8, we a slight modification to the DILATELINE function (line 13) to return the *extruded* seeds on the current sweepline instead of the dilated ones.

**2D Power Diagram.** In the rest of the discussion, we now focus on computing the 2D dilation of a shape  $S$  comprised of non-overlapping segments associated with a dilation radius  $(s_i^{\perp}, s_i^{\perp}; r_i)$ . In this setting, the computation of the power cells  $\Omega_i^p$  of seed segments becomes much more involved, and breaks some of the assumptions of our sweepline algorithm Figure 8. More specifically, our sweepline algorithm for Voronoi diagram makes the following assumptions about  $\mathcal{L}$ : the seeds projected on the sweepline are non-overlapping segments, and the Voronoi cells induced by the active seeds are *continuous* regions. Once a seed  $(s_i^{\perp}, s_i^{\perp})$  is inserted in  $\mathcal{L}$ , its cell  $\vec{\Omega}_i$  immediately becomes *active*, and once we reach the first removal event in  $\mathcal{Q}$ , it will become *inactive* and stop contributing to the dilation  $\vec{\mathcal{D}}(S)$ . For the power cells of *segments*, the situation is a little bit different, as illustrated on Figure 10: a power cell  $\vec{\Omega}_i^p$  can contain *disjoint* regions of the plane. It is not clear how to maintain a disjoint set of seeds in  $\mathcal{L}$  if we need to start removing and inserting a seed multiple time, and this makes the number of cases to consider grow significantly.

Instead, we propose to circumvent the problem entirely by making the following observation. A 2D segment dilated by a radius  $r$  is in fact a capsule, which can be described by two half-disks at the endpoints, and a rectangle in the middle. We decompose the half-dilated shape  $\vec{\mathcal{D}}^b(S)$  into the union of two different shapes:  $\vec{\mathcal{D}}^o(S)$ , the result of the half-dilation of each endpoint; and  $\vec{\mathcal{D}}^{\square}(S)$ , where each segment

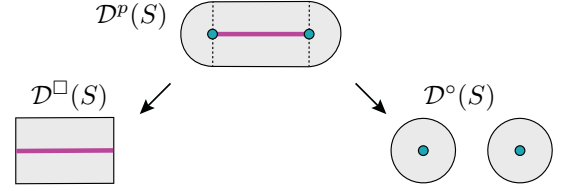


Fig. 11. To facilitate the computation of the power diagram in the second stage, the dilation of a segment is separated into a vertical extrusion (left), and the dilation of its two endpoints (right).

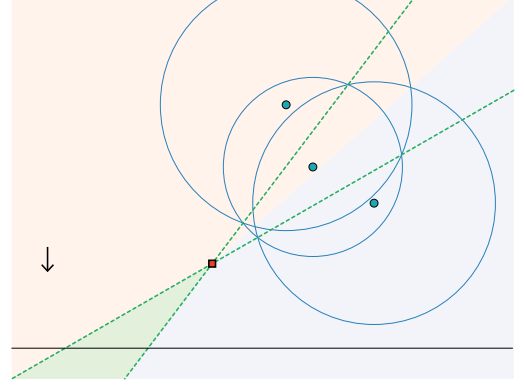


Fig. 12. Sweepline algorithm computing  $\vec{\mathcal{D}}^o(S)$ . When inserting the rightmost point in the set of active seeds  $\mathcal{L}$ , it may happen that the power vertex with its two neighbors be located further away along the sweep direction. In this case, the middle point should not be removed from  $\mathcal{L}$ , as its power cell will continue to intersect the sweepline.

$s_i$  is extruded along the dilation axis by its radius  $r_i$ . This decomposition is illustrated in Figure 11.

Now, the dilated shape  $\vec{\mathcal{D}}^{\square}(S)$  is easy to compute with a forward sweep, as there no Voronoi diagram or power diagram involved: we simply remove occluded subsegments, keeping the ones with the largest radius, and removing a seed  $s_i$  once its distance to the sweepline is  $> r_i$ . To compute  $\vec{\mathcal{D}}^o(S)$ , we employ a sweep similar to the one described Section 3.2, but now all the seeds are *points*, which greatly simplifies the calculation of power vertices. Indeed, the power bisectors are now lines, and the power cells are intersections of half-spaces, and in particular convex. The derivations for the coordinates of a power vertex is given in Appendix B. The only special case to consider here is illustrated in Figure 12: when inserting a new seed and updating  $\mathcal{L}$ , the events corresponding to a power vertex do not always correspond to a removal. For example, in the situation illustrated in Figure 12, the power cell of the middle point will continue to intersect the sweepline after it has passed the power vertex, so we should not remove the middle seed from  $\mathcal{L}$ . Fortunately, this case is easy to detect, and we simply forgo inserting the event in  $\mathcal{Q}$  in the first place.

### 3.4 Complexity Analysis

We analyze the runtime complexity of our algorithm for our first 2D dilation operation. For the purpose of this analysis, we assume that the dexel spacing is 1, so that the dilation

radius  $r$  is given in the same unit as the dixel numbers. The complexity of combining two dixel data structures is linear in the size of the input, since the segments are already sorted. Thus, we focus on analyzing the cost of the forward dilation operation  $\vec{D}_r(S)$ .

Let  $n$  be the number of input segments, and  $m$  be the number of output segments in the dilated shape  $\vec{D}(S)$ . In the worst case, each input segment generates  $\mathcal{O}(r)$  distinct output segments, and  $m = \mathcal{O}(nr)$ . In the worst case, each seed segment is split twice by every newly inserted segment. Since each seed can split in two separate segments at most one element of  $\mathcal{L}$ , so we have at any time that  $|\mathcal{L}| = \mathcal{O}(n)$ . Moreover, each seed produces at most three events in  $\mathcal{Q}$  (a Voronoi vertex with its left/right neighbors, and the moment it becomes inactive because of its distance to the sweepline). It follows that  $|\mathcal{Q}| = \mathcal{O}(n)$  as well. Segments in  $\mathcal{L}$  are stored in a `std::set<>`, thus insertion and removal (lines 7 and 10) can be performed in  $\mathcal{O}(\log n)$  time. While the line dilation (line 13) is linear in the size of  $\mathcal{L}$ , the total number of segments produced by this line cannot exceed  $m$ , so the amortized time complexity over the whole sweep is also  $\mathcal{O}(m)$ . This brings the final cost of the whole dilation algorithm to a time complexity that is  $\mathcal{O}(n \log(n) + m)$ , and it does not depend on the dilation radius  $r$  (apart from the output size  $m$ ). In comparison, the offsetting algorithm presented in [9] has a total complexity that grows proportionally to  $r^2$ .

For the second dilation operation, where each input segment is associated a specific dilation radius, the result is similar. Indeed,  $\vec{D}(S)$  is computed using the same algorithm as before, so the analysis still holds. Combining the dexels in  $\vec{D}(S)$  with the results from  $\vec{D}^\square(S)$  can be done linearly in the size of the output as we advance the sweepline, so the total complexity of computing  $\vec{D}^\flat(S)$  is still  $\mathcal{O}(n \log(n) + m)$ .

For the 3D case, the result of a first extrusion is used as input for the second stage dilation, the total complexity is more difficult to analyze, as it also depends on the structure of the intermediate result. In a very conservative estimate, bounding the number of intermediate segments by  $\mathcal{O}(nr)$ , this bring the final complexity of the 3D dilation to  $\mathcal{O}(nr \log(nr) + m)$ , where  $m = \mathcal{O}(nr^2)$  is the size of the output model. In practice, a lot of segments can be merged in the final output, especially when the dilation radius is large, and  $m$  may even be smaller than  $n$  (e.g. when details are erased from the surface).

Finally, we note that in each stage of the 3D pipeline, the 2D dilations can be performed completely independently in every slice of the dixel structure, making the process trivial to parallelize. We discuss in Section 4 the experimental performances of our a multi-threaded implementation of our 3D dilation operation.

## 4 RESULTS

We implemented our algorithm in C++ using Eigen for linear algebra routines, and Intel Threading Building Blocks for parallelization. We ran our experiments on a desktop with a 6-core Intel® Core™ i7-5930K CPU clocked at 3.5 GHz and

64 GB of memory. The reference implementation, equipped with scripts to reproduce all our results, is attached as addition material and will be released as an open-source project to facilitate the adoption of our technique.

**Baseline Comparison.** We implemented a simple brute-force dilation algorithm (on the dixel grid) to verify the correctness of our implementation, and to demonstrate the benefits of our technique. In the brute-force algorithm, each segment in the input dixel structure generates an explicit list of dilated segments in a disk of radius  $r$  around it, and all overlapping segments are merged in the output data structure. Figure 13 compares the two methods using a different number of threads, and with respect to both grid size and dilation radius. In all cases, our algorithm is superior not only asymptotically, but also for a fixed grid size or dilation radius. Since each slice can be treated independently in our two-stage dilation process, our algorithm is embarrassingly parallel, and scales almost linearly with the number of threads used.

We note that the asymptotic time complexity observed in Figure 13 agrees with our analysis in Section 3.4. Indeed, the dixel grid has a number of dixel  $n \propto s^2$  is proportional to the squared grid size  $s^2$ , while the (absolute) dilation radius  $r_{\text{abs}} \propto sr_{\text{rel}}$  grows linearly with the grid size. Since the complexity analysis in Section 3.4 uses a dilation radius  $r$  expressed in dixel units, the observed asymptotic rate of  $\approx 3$  for indicates that our method is indeed  $\mathcal{O}(s^3)$ .

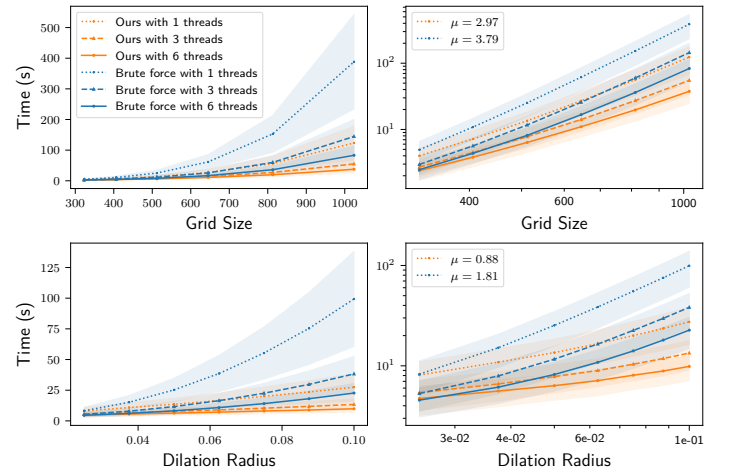


Fig. 13. Total running time averaged on 11 testing models, compared with a direct brute-force implementation. Standard deviation is shown in overlay, and convergence rate  $\mu$  are reported in the log-log plots. Radii are relative to the grid size. The top row uses a relative radius of 0.05, and the bottom row uses a grid size of  $512^2$ .

**Dilation vs Erosion.** In Figure 14, we compare the performance of the dilation and erosion operator on a small dataset of 11 models, provided in the supplemental material. The dilation operator has a higher cost than the erosion, both asymptotically and in absolute running time. This is likely due to the fact that the erosion operator reduces the number of dexels in the data structure, leading to a clear speedup.

**Comparison with Wang *et al.* [9].** The most closely related work on offset from ray-reps representations is Wang *et al.* [9]. It proposes to perform an offset from a LDI sampled



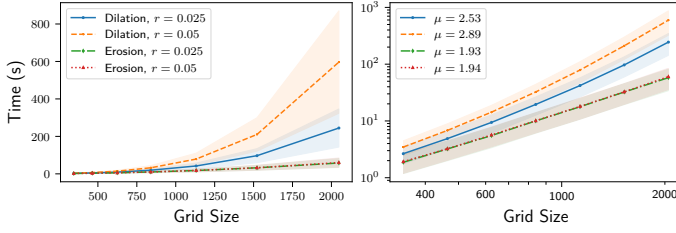


Fig. 14. Total running time of the dilation vs erosion operation, for two different radii. Standard deviation shown in overlay and convergence rate  $\mu$  reported in the log-log plot.

from three orthogonal directions. The offset is computed as the union of spheres sampled at the endpoints of each segment from all three directions at once. In contrast, our method relies on a single dixel structure, which has both advantages and drawbacks: it is applicable in a situation where only one view is available, or is enough to describe the model (e.g. modeling for additive manufacturing [12]), but it will be less precise on the orthogonal directions (where the 3-views LDI will have more precise samples).

To compare our method with theirs, we matched the parameters of the experiment reported in Table 2 of [9], and compare our results with the 4-thread CPU version reported in [9]. At a resolution of  $512^2$  and relative radius of 0.025 the diagonal of the bounding box, our running time was 3.4s, 3.7s, and 2.7s for the Vase-lion, Filigree, and Buddha models respectively. The timings reported in [9] for their CPU implementation are over 120s, suggesting that our CPU implementation is competitive even with their GPU implementation. Extending our method to the GPU will be challenging, but could enable real-time offsetting on large and complex dixel structures, which we believe would be an interesting venue for future work.

**Topological Cleaning.** Our efficient dilation and erosion operators can be combined to obtain efficient opening and closing operators (Figure 15). For example, the closing operation can be used to remove topological noise, i.e. small handles, by first dilating the shape by a fixed offset, and then partially undoing it using erosion. While most parts of the shape will recover their original shape, small holes and sharp features will not, providing an effective way to simplify the shape topology.

**Scalability.** The compactness of the dixel representation enables us to represent and process immense volumes on normal desktop computers. An example is shown in Figure 16 for the erosion operation. Note that the results on the right have a resolution sufficiently high to hide the dexels: this resolution would be prohibitive with a traditional boundary or voxel representation.

**3D Printing.** The Boolean difference between a dilation and erosion of a shape produces a shell (of controllable thickness). This operation is common for 3D printing applications, since the interior of an object is usually left void (or filled with support structures) to save material. Another typical use-case for creating thick shells out of a surface mesh is the creation of molds [36]. We show a high resolution example

in Figure 1, which has been 3D printed using PLA plastic on a Ultimaker 3 printer.

## 5 FUTURE WORK AND CONCLUDING REMARKS

Our current implementation is restricted to uniform morphological operations, and it would be interesting to extend it to single direction thickening (for example in the normal direction only) or to directly work on a LDI offset, i.e. representing the shape with 3 dixel representations, one for each axis. A GPU implementation of our technique would likely provide a sufficient speedup to enable real-time processing of ray-reps representation at the resolution typically used by modern 3D printers.

To conclude, we proposed an algorithm to efficiently compute morphological operations on ray-rep representations, targeting in particular the generation of surface offsets. Beside offering theoretical insights on power diagrams and their application to surface offsets, our algorithm is simple, robust, and efficient: it is an ideal tool in 3D printing applications, since it can directly process voxel or dixel representations to filter out topological noise or extract volumetric shells from boundary representations.

## ACKNOWLEDGMENTS

This work was supported in part by the NSF CAREER award IIS-1652515, a gift from Adobe, and a gift from nTopology.

## REFERENCES

- [1] J. Williams and J. Rossignac, “Mason: Morphological simplification,” *Graphical models*, vol. 67, no. 4, pp. 285–303, Jul. 2005. DOI: [10.1016/j.gmod.2004.10.001](https://doi.org/10.1016/j.gmod.2004.10.001).
- [2] O. Sigmund, “Morphology-based black and white filters for topology optimization,” *Structural and multidisciplinary optimization*, vol. 33, no. 4-5, pp. 401–424, Jan. 2007. DOI: [10.1007/s00158-006-0087-x](https://doi.org/10.1007/s00158-006-0087-x).
- [3] M. Teschner, S. Kimmerle, B. Heidelberger, G. Zachmann, L. Raghupathi, A. Fuhrmann, M. P. Cani, F. Faure, N. Magnenat-Thalmann, W. Strasser, and P. Volino, “Collision detection for deformable objects,” *Computer graphics forum*, vol. 24, no. 1, pp. 61–81, Mar. 2005. DOI: [10.1111/j.1467-8659.2005.00829.x](https://doi.org/10.1111/j.1467-8659.2005.00829.x).
- [4] P. Maragos and R. Schafer, “Morphological skeleton representation and coding of binary images,” *Ieee transactions on acoustics, speech, and signal processing*, vol. 34, no. 5, pp. 1228–1244, Oct. 1986. DOI: [10.1109/tassp.1986.1164959](https://doi.org/10.1109/tassp.1986.1164959).
- [5] M. Livesu, S. Ellero, J. Martínez, S. Lefebvre, and M. Attene, “From 3D models to 3D prints: An overview of the processing pipeline,” *Computer graphics forum*, vol. 36, no. 2, pp. 537–564, May 2017. DOI: [10.1111/cgf.13147](https://doi.org/10.1111/cgf.13147).
- [6] S. Hornus, S. Lefebvre, J. Dumas, and F. Claux, “Tight printable enclosures and support structures for additive manufacturing,” in *Eurographics workshop on graphics for digital fabrication*, The Eurographics Association, 2016, ISBN: 978-3-03868-003-1. DOI: [10.2312/gdf.20161074](https://doi.org/10.2312/gdf.20161074).



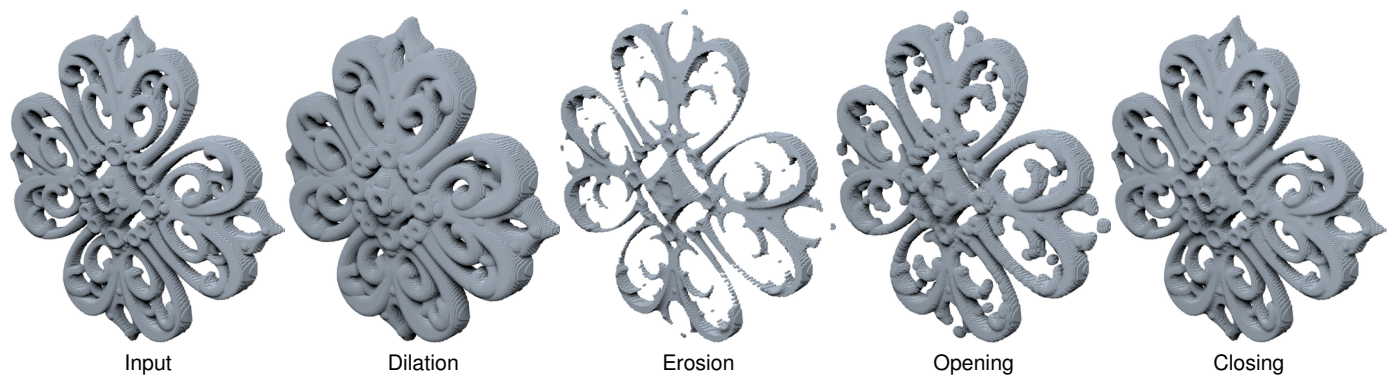


Fig. 15. Topological cleaning of an input shape via morphological operations, using a grid of  $256 \times 256$  dexels.

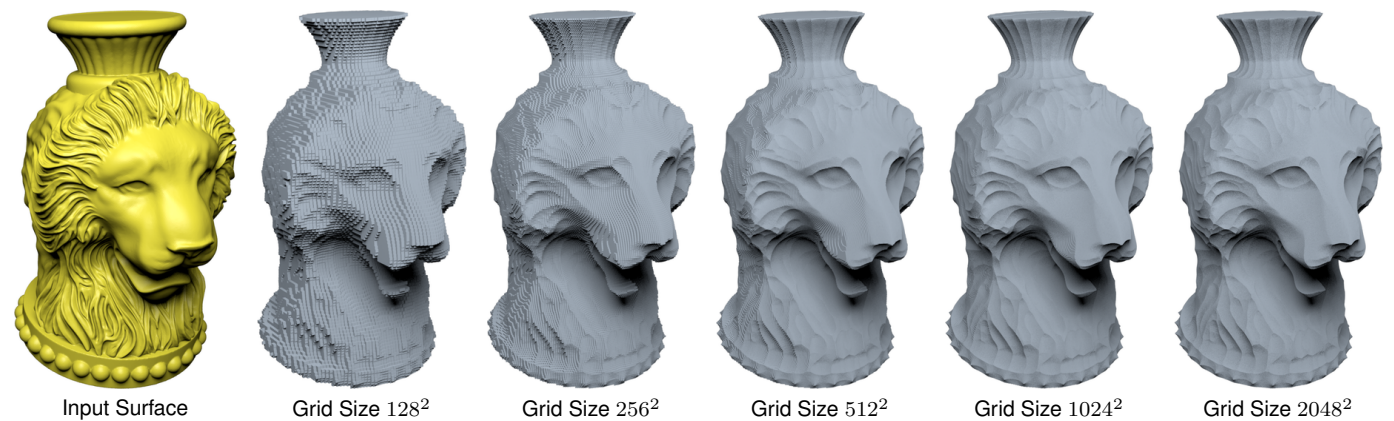


Fig. 16. Result of an erosion operation using different grid resolutions.

- [7] P. Hachenberger, "Exact minkowski sums of polyhedra and exact and efficient decomposition of polyhedra in convex pieces," in *Proceedings of the 15th annual european conference on algorithms*, ser. ESA'07, Eilat, Israel: Springer-Verlag, 2007, pp. 669–680.
- [8] W. Meng, S. Chen, Z. Shu, S.-Q. Xin, H. Fu, and C. Tu, "Efficiently computing feature-aligned and high-quality polygonal offset surfaces," *Computers & graphics*, Jul. 2017. DOI: [10.1016/j.cag.2017.07.003](https://doi.org/10.1016/j.cag.2017.07.003).
- [9] C. C. L. Wang and D. Manocha, "Gpu-based offset surface computation using point samples," *Computer-aided design*, vol. 45, no. 2, pp. 321–330, Feb. 2013. DOI: [10.1016/j.cad.2012.10.015](https://doi.org/10.1016/j.cad.2012.10.015).
- [10] J. Martínez, S. Hornus, F. Claux, and S. Lefebvre, "Chained segment offsetting for ray-based solid representations," *Computers & graphics*, vol. 46, pp. 36–47, Feb. 2015. DOI: [10.1016/j.cag.2014.09.017](https://doi.org/10.1016/j.cag.2014.09.017).
- [11] T. Van Hook, "Real-time shaded nc milling display," in *Proceedings of the 13th annual conference on computer graphics and interactive techniques - siggraph '86*, Association for Computing Machinery (ACM), 1986. DOI: [10.1145/15922.15887](https://doi.org/10.1145/15922.15887).
- [12] S. Lefebvre, "Icesl: A gpu accelerated csg modeler and slicer," in *AeFA'13, 18th european forum on additive manufacturing*, 2013. eprint: <http://webloria.loria.fr/~slefebvr/icesl/icesl-whitepaper.pdf>.
- [13] C. Fan, J. Luo, J. Liu, and Y. Xu, "Half-plane voronoi diagram," in *2011 eighth international symposium on voronoi diagrams in science and engineering*, Institute of Electrical & Electronics Engineers (IEEE), Jun. 2011. DOI: [10.1109/isvd.2011.25](https://doi.org/10.1109/isvd.2011.25).
- [14] A. Meijster, J. B.T. M. Roerdink, and W. H. Hesselink, "A general algorithm for computing distance transforms in linear time," in *Mathematical morphology and its applications to image and signal processing*, Kluwer Academic Publishers, 2002, pp. 331–340. DOI: [10.1007/0-306-47025-x\\_36](https://doi.org/10.1007/0-306-47025-x_36).
- [15] W. Jung, H. Shin, and B. K. Choi, "Self-intersection removal in triangular mesh offsetting," *Computer-aided design and applications*, vol. 1, no. 1-4, pp. 477–484, Jan. 2004. DOI: [10.1080/16864360.2004.10738290](https://doi.org/10.1080/16864360.2004.10738290).
- [16] M. Campen and L. Kobbelt, "Polygonal boundary evaluation of minkowski sums and swept volumes," *Computer graphics forum*, vol. 29, no. 5, pp. 1613–1622, Sep. 2010. DOI: [10.1111/j.1467-8659.2010.01770.x](https://doi.org/10.1111/j.1467-8659.2010.01770.x).
- [17] G. Varadhan and D. Manocha, "Accurate minkowski sum approximation of polyhedral models," *Graphical models*, vol. 68, no. 4, pp. 343–355, Jul. 2006. DOI: [10.1016/j.gmod.2005.11.003](https://doi.org/10.1016/j.gmod.2005.11.003).
- [18] M. Peternell and T. Steiner, "Minkowski sum boundary surfaces of 3d-objects," *Graphical models*, vol. 69, no. 3-4, pp. 180–190, May 2007. DOI: [10.1016/j.gmod.2007.01.001](https://doi.org/10.1016/j.gmod.2007.01.001).
- [19] S. Calderon and T. Boubekeur, "Point morphology," *Acm transactions on graphics*, vol. 33, no. 4, pp. 1–13, Jul. 2014. DOI: [10.1145/2601097.2601130](https://doi.org/10.1145/2601097.2601130).

- [20] Y. Liu, W. Wang, B. Lévy, F. Sun, D.-M. Yan, L. Lu, and C. Yang, "On centroidal voronoi tessellation—energy smoothness and fast computation," *Acm transactions on graphics*, vol. 28, no. 4, pp. 1–17, Aug. 2009. DOI: [10.1145/1559755.1559758](https://doi.org/10.1145/1559755.1559758).
- [21] S.-Q. Xin, B. Lévy, Z. Chen, L. Chu, Y. Yu, C. Tu, and W. Wang, "Centroidal power diagrams with capacity constraints," *Acm transactions on graphics*, vol. 35, no. 6, pp. 1–12, Nov. 2016. DOI: [10.1145/2980179.2982428](https://doi.org/10.1145/2980179.2982428).
- [22] S. Fortune, "A swepline algorithm for voronoi diagrams," *Algorithmica*, vol. 2, no. 1–4, pp. 153–174, Nov. 1987. DOI: [10.1007/bf01840357](https://doi.org/10.1007/bf01840357).
- [23] F. Aurenhammer, "Power diagrams: Properties, algorithms and applications," *Siam journal on computing*, vol. 16, no. 1, pp. 78–96, Feb. 1987. DOI: [10.1137/0216006](https://doi.org/10.1137/0216006).
- [24] L. Lu, B. Lévy, and W. Wang, "Centroidal voronoi tessellation of line segments and graphs," *Computer graphics forum*, vol. 31, no. 2pt4, pp. 775–784, May 2012. DOI: [10.1111/j.1467-8659.2012.03058.x](https://doi.org/10.1111/j.1467-8659.2012.03058.x).
- [25] C. R. Maurer, R. Qi, and V. Raghavan, "A linear time algorithm for computing exact euclidean distance transforms of binary images in arbitrary dimensions," *Ieee transactions on pattern analysis and machine intelligence*, vol. 25, no. 2, pp. 265–270, Feb. 2003. DOI: [10.1109/tpami.2003.1177156](https://doi.org/10.1109/tpami.2003.1177156).
- [26] R. Fabbri, L. D. F. Costa, J. C. Torelli, and O. M. Bruno, "2d euclidean distance transform algorithms: A comparative survey," *Acm computing surveys*, vol. 40, no. 1, pp. 1–44, Feb. 2008. DOI: [10.1145/1322432.1322434](https://doi.org/10.1145/1322432.1322434).
- [27] J. Shade, S. Gortler, L.-w. He, and R. Szeliski, "Layered depth images," in *Proceedings of the 25th annual conference on computer graphics and interactive techniques - siggraph '98*, Association for Computing Machinery (ACM), 1998. DOI: [10.1145/280814.280882](https://doi.org/10.1145/280814.280882).
- [28] L. Carpenter, "The a-buffer, an antialiased hidden surface method," in *Proceedings of the 11th annual conference on computer graphics and interactive techniques - siggraph '84*, Association for Computing Machinery (ACM), 1984. DOI: [10.1145/800031.808585](https://doi.org/10.1145/800031.808585).
- [29] M. Maule, J. L. Comba, R. P. Torchelsen, and R. Bastos, "A survey of raster-based transparency techniques," *Computers & graphics*, vol. 35, no. 6, pp. 1023–1034, Dec. 2011. DOI: [10.1016/j.cag.2011.07.006](https://doi.org/10.1016/j.cag.2011.07.006).
- [30] T. Saito and T. Takahashi, "Nc machining with g-buffer method," *Acm siggraph computer graphics*, vol. 25, no. 4, pp. 207–216, Jul. 1991. DOI: [10.1145/127719.122741](https://doi.org/10.1145/127719.122741).
- [31] C. C. L. Wang, Y.-S. Leung, and Y. Chen, "Solid modeling of polyhedral objects by layered depth-normal images on the gpu," *Computer-aided design*, vol. 42, no. 6, pp. 535–544, Jun. 2010. DOI: [10.1016/j.cad.2010.02.001](https://doi.org/10.1016/j.cad.2010.02.001).
- [32] P. Huang, C. C. L. Wang, and Y. Chen, "Algorithms for layered manufacturing in image space," in *Advances in computers and information in engineering research, volume 1*, ASME Press, 2014. DOI: [10.1115/1.860328\\_ch15](https://doi.org/10.1115/1.860328_ch15).
- [33] E. E. Hartquist, J. P. Menon, K. Suresh, H. B. Voelcker, and J. Zagajac, "A computing strategy for applications involving offsets, sweeps, and minkowski operations," *Computer-aided design*, vol. 31, no. 3, pp. 175–183, Mar. 1999. DOI: [10.1016/s0010-4485\(99\)00014-7](https://doi.org/10.1016/s0010-4485(99)00014-7).
- [34] K. C. Hui, "Solid sweeping in image space—application in nc simulation," *The visual computer*, vol. 10, no. 6, pp. 306–316, Jun. 1994. DOI: [10.1007/bf01900825](https://doi.org/10.1007/bf01900825).
- [35] Y. Chen and C. C. L. Wang, "Uniform offsetting of polygonal model based on layered depth-normal images," *Computer-aided design*, vol. 43, no. 1, pp. 31–46, Jan. 2011. DOI: [10.1016/j.cad.2010.09.002](https://doi.org/10.1016/j.cad.2010.09.002).
- [36] L. Malomo, N. Pietroni, B. Bickel, and P. Cignoni, "Flexmolds: Automatic design of flexible shells for molding," *Acm transactions on graphics*, vol. 35, no. 6, pp. 1–12, Nov. 2016. DOI: [10.1145/2980179.2982397](https://doi.org/10.1145/2980179.2982397).



**Zhen Chen** is working towards his bachelor degree in Computational & Informational Science at University of Science and Technology of China (USTC), China. He will graduate at the beginning of June 2018. From June to August 2017, he has been a visiting student at the Courant Institute of Mathematical Sciences (New York University, USA). His research interests are 3D printing and geometry processing.



**Daniele Panozzo** Daniele Panozzo is an assistant professor of computer science at the Courant Institute of Mathematical Sciences in New York University. Prior to joining NYU he was a postdoctoral researcher at ETH Zurich (2012–2015). He earned his PhD in Computer Science from the University of Genova (2012) and his doctoral thesis received the EUROGRAPHICS Award for Best PhD Thesis (2013). He received the EUROGRAPHICS Young Researcher Award in 2015 and the NSF CAREER Award in 2017.

Daniele is leading the development of libigl (<https://github.com/libigl/libigl>), an award-winning (EUROGRAPHICS Symposium of Geometry Processing Software Award, 2015) open-source geometry processing library that supports academic and industrial research and practice. Daniele is chairing the Graphics Replicability Stamp (<http://www.replicabilitystamp.org>), which is an initiative to promote reproducibility of research results and to allow scientists and practitioners to immediately benefit from state-of-the-art research results. Daniele's research interests are in digital fabrication, geometry processing, architectural geometry, and discrete differential geometry.



**Jérémie Dumas** Jérémie Dumas is a postdoctoral fellow at the Courant Institute of Mathematical Sciences in New York University. Prior to joining NYU he completed his PhD at INRIA Nancy Grand-Est (2017), under the direction of Sylvain Lefebvre. His doctoral thesis received the EUROGRAPHICS Award for Best PhD Thesis (2018). His work focuses on shape synthesis for digital fabrication, including shape optimization, simulation, microstructures, and procedural synthesis.

## APPENDIX A

### VORONOI VERTEX BETWEEN THREE PARALLEL SEGMENTS IN 2D

The bisector of two parallel segment seeds in 2D is a piecewise-quadratic curve, as illustrated in Figure 7. A Voronoi vertex is a point at the intersection of the bisector curves between three segment seeds. Because the segment seeds are non-overlapping, the Voronoi vertex can be either between three points (Section A.1) or between one segment and two points (Section A.2).

#### A.1 Voronoi Vertex between Three Points

Let  $p_1, p_2, p_3$  be three points, with coordinates  $p_i = (y_i, z_i)$ . A point  $p$  lying on the bisector of  $(p_1, p_2)$  satisfies

$$\begin{aligned} \|p - p_1\|^2 &= \|p - p_2\|^2 \\ \iff (y - y_1)^2 + (z - z_1)^2 &= (y - y_2)^2 + (z - z_2)^2 \end{aligned} \quad (7)$$

After simplification, we get

$$2(y_2 - y_1)y + 2(z_2 - z_1)z = (y_2^2 + z_2^2) - (y_1^2 + z_1^2) \quad (8)$$

Similarly, for a point lying on the bisector of  $(p_2, p_3)$ ,

$$2(y_3 - y_2)y + 2(z_3 - z_2)z = (y_3^2 + z_3^2) - (y_2^2 + z_2^2) \quad (9)$$

We can get the coordinate of Voronoi vertex between three points by solving the system formed by Equations (8) and (9):

$$2 \begin{pmatrix} y_2 - y_1 & z_2 - z_1 \\ y_3 - y_2 & z_3 - z_2 \end{pmatrix} \begin{pmatrix} y \\ z \end{pmatrix} = \begin{pmatrix} (y_2^2 + z_2^2) - (y_1^2 + z_1^2) \\ (y_3^2 + z_3^2) - (y_2^2 + z_2^2) \end{pmatrix} \quad (10)$$

#### A.2 Voronoi Vertex between a Segment and Two Points

Let  $p_1(y_1, z_1), s(y_s, z_s^+, z_s^-), p_2(y_2, z_2)$  be three seeds. We only need to consider the case where  $y_s < y_1 < y_2$ , other cases are similar. For the Voronoi vertex  $p = (y, z)$  to intersect the bisectors where it is closest to the interior of  $s$ , and not one its endpoints, we need to have  $z_s^+ < z < z_s^-$ . It follows the distance from  $p$  to the segment  $s$  is:

$$\begin{aligned} \text{dist}(p, s) &= \inf_{(a,b) \in s} (y - a)^2 + (z - b)^2 \\ &= (y - y_s)^2 \quad \text{when } (a, b) = (y_s, z) \end{aligned} \quad (11)$$

By definition of the Voronoi vertex,

$$\text{dist}(p, s) = \text{dist}(p, p_1) \quad (12)$$

$$\text{dist}(p, p_1) = \text{dist}(p, p_2) \quad (13)$$

Developing Equation (12), we get

$$\begin{aligned} (y - y_s)^2 &= (y - y_1)^2 + (z - z_1)^2 \\ \iff 2(y_1 - y_s)y - (z - z_1)^2 &= z_1^2 - y_s^2 \end{aligned} \quad (14)$$

Similarly, developing Equation (13) leads to

$$2(y_1 - y_2)y + 2(z_1 - z_2)z = (y_1^2 + z_1^2) - (y_2^2 + z_2^2) \quad (15)$$

Now, let

$$\begin{cases} u = 2(y_1 - y_s) \\ w = -y_1^2 + y_s^2 \\ a = 2(y_1 - y_2) \\ b = 2(z_1 - z_2) \\ c = (y_1^2 + z_1^2) - (y_2^2 + z_2^2) \end{cases}$$

We can rewrite the system of equations as

$$\begin{cases} uy - (z - z_1)^2 + w = 0 \\ ay + bz = c \end{cases} \quad (16)$$

$$\implies az^2 + (bu - 2az_1)y + az_1 - cu - aw = 0 \quad (17)$$

Solving Equation (17), if the roots exist, we will have

$$\begin{aligned} \Delta &= (bu - 2az_1)^2 - 4a(az_1^2 - cu - aw) \\ z_{1,2}^* &= \frac{2az_1 - bu \pm \sqrt{\Delta}}{2a} \end{aligned}$$

Choosing the solution that belongs to  $[z_s^+, z_s^-]$ , and substituting into  $ay + bz = c$ , we will get the  $y$ -coordinate of our Voronoi vertex.

## APPENDIX B

### POWER VERTEX BETWEEN THREE POINTS IN 2D

Let  $p_1(y_1, z_1; r_1), p_2(y_2, z_2; r_2), p_3(y_3, z_3; r_3)$  be three seeds. A power vertex can be computed from the intersection of two bisector lines.

A point  $p(y, z)$  lying on the bisector of  $(p_1, p_2)$  satisfies:

$$\begin{aligned} \|p - p_1\|^2 - r_1^2 &= \|p - p_2\|^2 - r_2^2 \\ \iff (y_1 - y)^2 + (z - z_1)^2 - r_1^2 &= (y_2 - y)^2 + (z - z_2)^2 - r_2^2 \\ \iff 2(y_2 - y_1)y + 2(z_2 - z_1)z &= (y_2^2 + z_2^2 - r_2^2) - (y_1^2 + z_1^2 - r_1^2) \end{aligned} \quad (18)$$

A similar equation holds for the bisector of  $(p_2, p_3)$ . This translates into the following system of equations:

$$2 \begin{pmatrix} y_2 - y_1 & z_2 - z_1 \\ y_3 - y_2 & z_3 - z_2 \end{pmatrix} \begin{pmatrix} y \\ z \end{pmatrix} = \begin{pmatrix} (y_2^2 + z_2^2 - r_2^2) - (y_1^2 + z_1^2 - r_1^2) \\ (y_3^2 + z_3^2 - r_3^2) - (y_2^2 + z_2^2 - r_2^2) \end{pmatrix} \quad (19)$$